ACCSCIENCE PUBLISHING

International Journal of Bioprinting

RESEARCH ARTICLE

Computational investigation of a 3D-printed osteochondral interface scaffold with comprehensive interfacial mechanical properties

Supplementary file

To estimate the mechanical properties of each 3D-printed osteochondral interface scaffold, self-designed testing devices were proposed in **Section 2.5**. Firstly, a tensile/compressive testing device was developed to investigate the interfacial bonding strength and compressive strength of the osteochondral interface scaffold (Figure S1A). Two vises were respectively fixed on a pressure sensor (Type 9256C1 SN1841599, KISTLER) and a linear stage (LX80-C311A6, SELN). In the tensile/compressive test, the cartilage and subchondral bone parts in the scaffold were held tightly by two vises separately. Secondly, to evaluate the interfacial shear strength of the biomimetic osteochondral interface, another interfacial shear device was also designed (Figure S1B). A vise was fixed on the top of the pressure sensor to hold the osteochondral interface scaffold. Meanwhile, an aluminum plate was bonded on the linear stage and utilized to shear the osteochondral scaffold at the interface.

In **Section 3.1.1.**, the stress contour plots of the first and third principal stresses for structures in the tensile process with various h have been obtained (Figures S2 and S3). Within each scaffold pattern, the stress distribution manifested obvious concentration near the bone–cartilage junction. The simulations revealed that the maxima of both the first and third principal stresses were localized at the filament of the bone structure, which was perpendicular to the tensile direction. The greatest tensile stress was concentrated on the side farthest away from the boundary load, while the maximum compressive stress was localized on the opposite side. Of all the scaffolds, the largest tensile and compressive stress showed decreasing tendencies with the improvement of h. Among the four patterns of scaffolds, the first and third principal stresses demonstrated an obvious reduction with the increase of h.

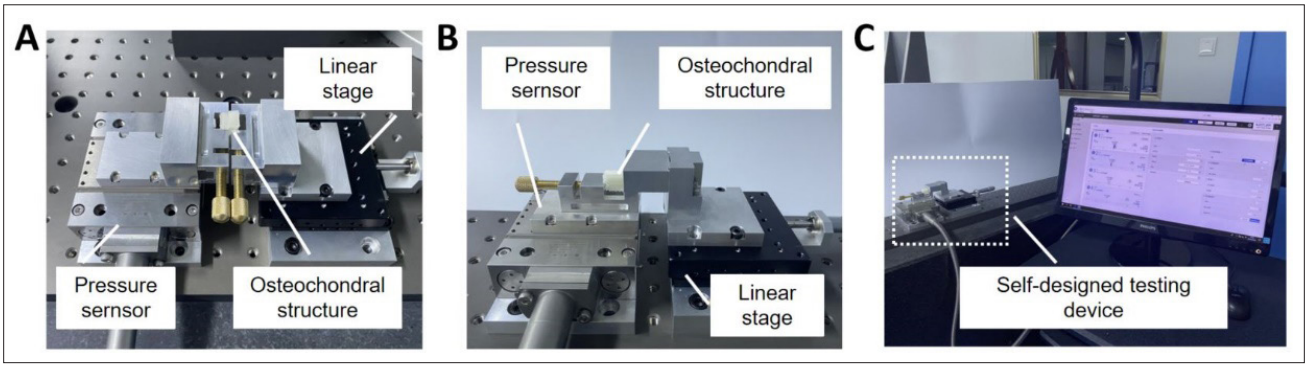

Figure S1. (A) A self-designed tensile/compressive testing device for investigating the interfacial bonding and compressive strengths of the osteochondral interface scaffold. (B) A self-designed interfacial shear testing device for investigating the interfacial shear strength and compressive strength of the biomimetic osteochondral interface units. (C) Experimental setup for tensile/compressive testing and shear testing.

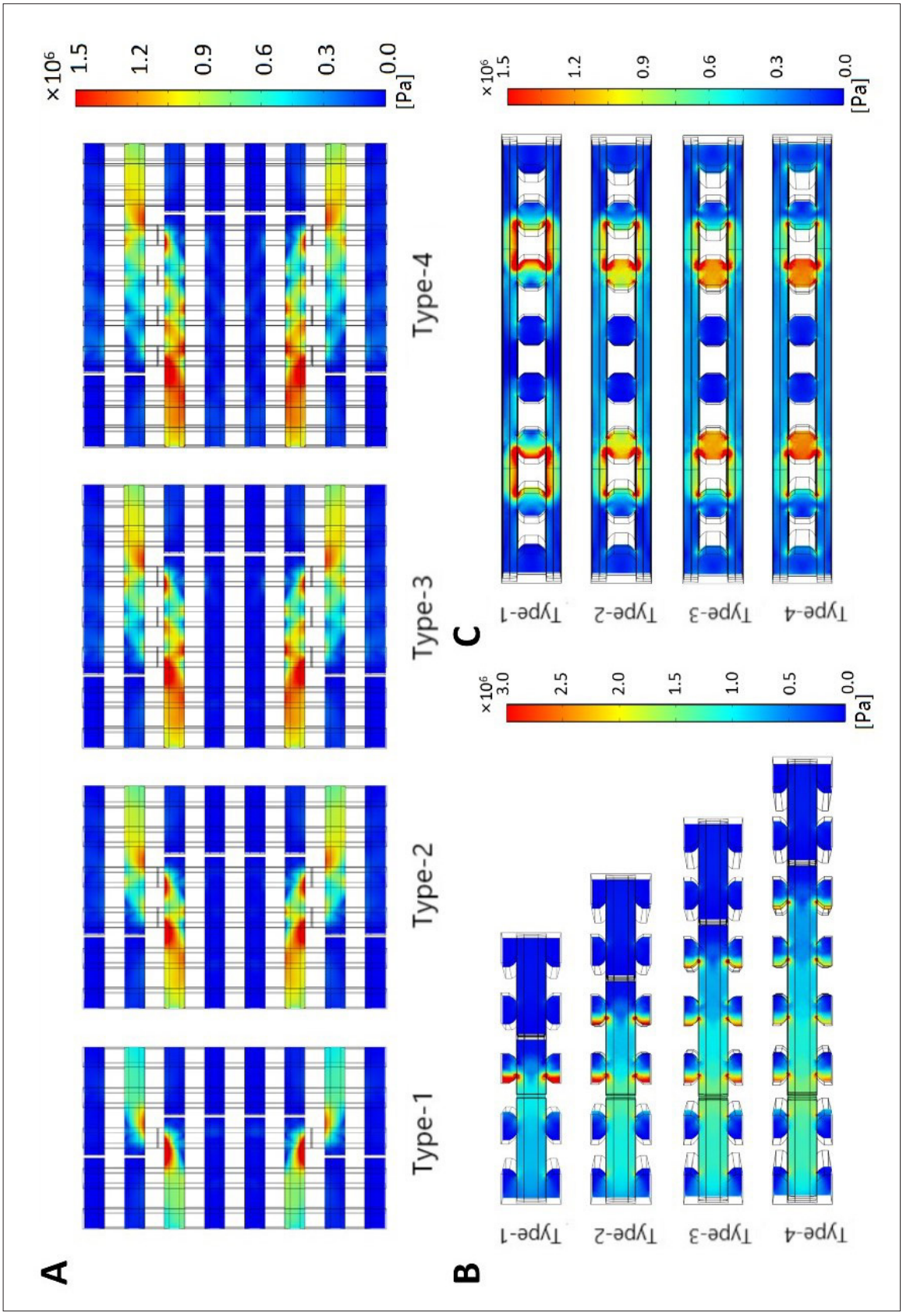

Figure S2. The stress contour plots of the first principal stress for structures with various heights of pin (*h*) in the tensile process. (A) Stress contour plots for the cross-section α. (B) Stress contour plots for the cross-section β. The greatest tensile stress is concentrated on the side farthest away from the boundary load. (C) Stress contour plots for the cross-section δ. Filaments near the bone–cartilage junction, which are along and perpendicular to the tensile direction, show a stress concentration at each fusion.

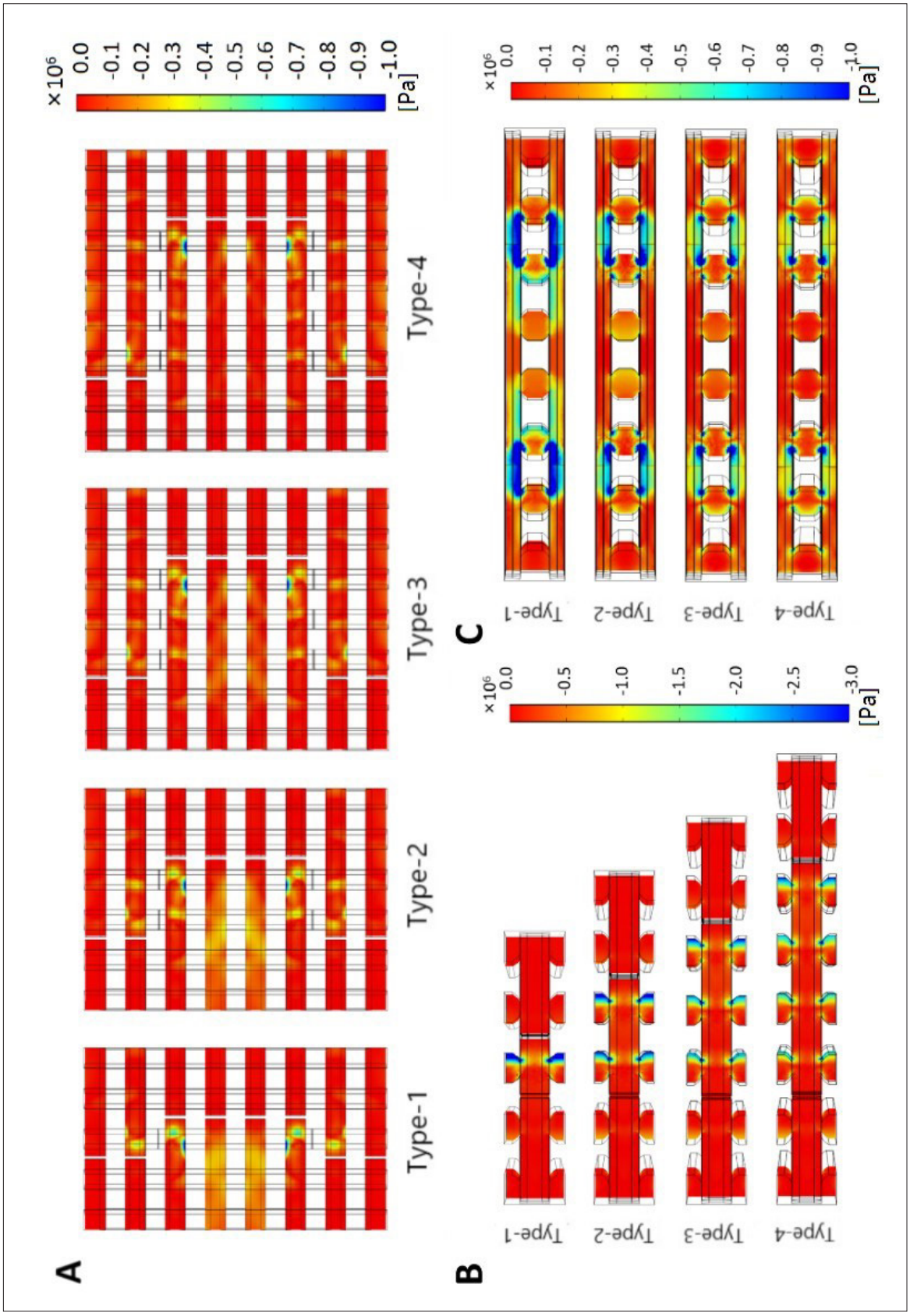

Figure S3. The stress contour plots of the third principal stress for structures with various heights of pin (*h*) in the tensile process. (A) Stress contour plots for the cross-section α in the tensile process. (B) Stress contour plots for the cross-section β. (C) Stress contour plots for the cross-section δ. Filaments show a stress concentration at each fusion.

The distribution of the first and the third principal stresses for designed scaffolds with various *w* was calculated (Figures S4 and S5). The locations of the greatest tensile and compressive stresses were consistent with the aforementioned results (Figures S2 and S3). Interestingly, the maximum values of both the first and the third principal stresses were nearly constant with the increase of *w*.

In **Section 3.1.2.**, the von Mises stress contour plots of the osteochondral interface scaffolds in the compressing process suggested a similar stress distribution as the simulation results in the tensile process (Figures S6 and S7). However, the stress contour plots of the first and third principal stresses of the compressing process indicated a dissimilar distribution with that of the tensile process (Figures S8 and S9).

The maximum tensile and compressive stresses were concentrated at the perpendicular filament to the compression direction. The greatest tensile stress was concentrated on the side farthest from the fixed constraint, while the largest compressive stress occurred on the closer side of the filament. The maximum values of both tensile and compressive stress decreased with an increase in *h* and showed minimal variations with changes in *w* (Figures S10 and S11).

In the simulation for the shearing process (**Section 3.1.3.**), stress contour plots of the first and third principal stresses were obtained for scaffolds of various *h* (Figures S12 and S13). Each pattern of scaffold experienced greater tensile and compressive stresses near the junction of the pin and the pedestal of the bone structure. The maximum stresses were concentrated at the surface of perpendicular filaments to the shear direction, and the location was close to their junctions with the outermost layer of bone structure. Of all the interface scaffolds, the greatest tensile and compressive stresses suggested few changes with varying *h*.

The first as well as third principal stress indicated a concentration at the pedestal of each bone structure (Figures S14 and S15) in the osteochondral interface scaffolds with varying *w*. The greatest tensile and compressive stresses occurred on the surface of the perpendicular filament to the shear direction. The largest magnitude of tensile stress was localized on the side farthest from the boundary load, while that of compressive stress was localized on the opposite side. This suggests that the maximum first and third principal stresses both exhibited a decrease with the increasing *w*.

To explain the phenomena of stress distributions, deformation contour plots for the structures were calculated (**Section 4.1.**). In the tensile process, the region of the scaffold near the boundary load manifested a shrinkage, while the region near the pedestal of the bone structure expanded (Figures S16 and S17). The bending of these filaments led to the concentration of principal and von Mises stresses. In the compressing process, the scaffold region near the boundary load exhibited an expansion, while shrinkage occurred at the scaffold close to the bottom of the pin structure (Figures S18 and S19). In the shearing process, the entire cartilage and the pin showed a deformation along the shear direction (Figures S20 and S21). This generated a bending at the bottom of each pin, which led to a stress concentration at the surface of filaments perpendicular to the shear direction.

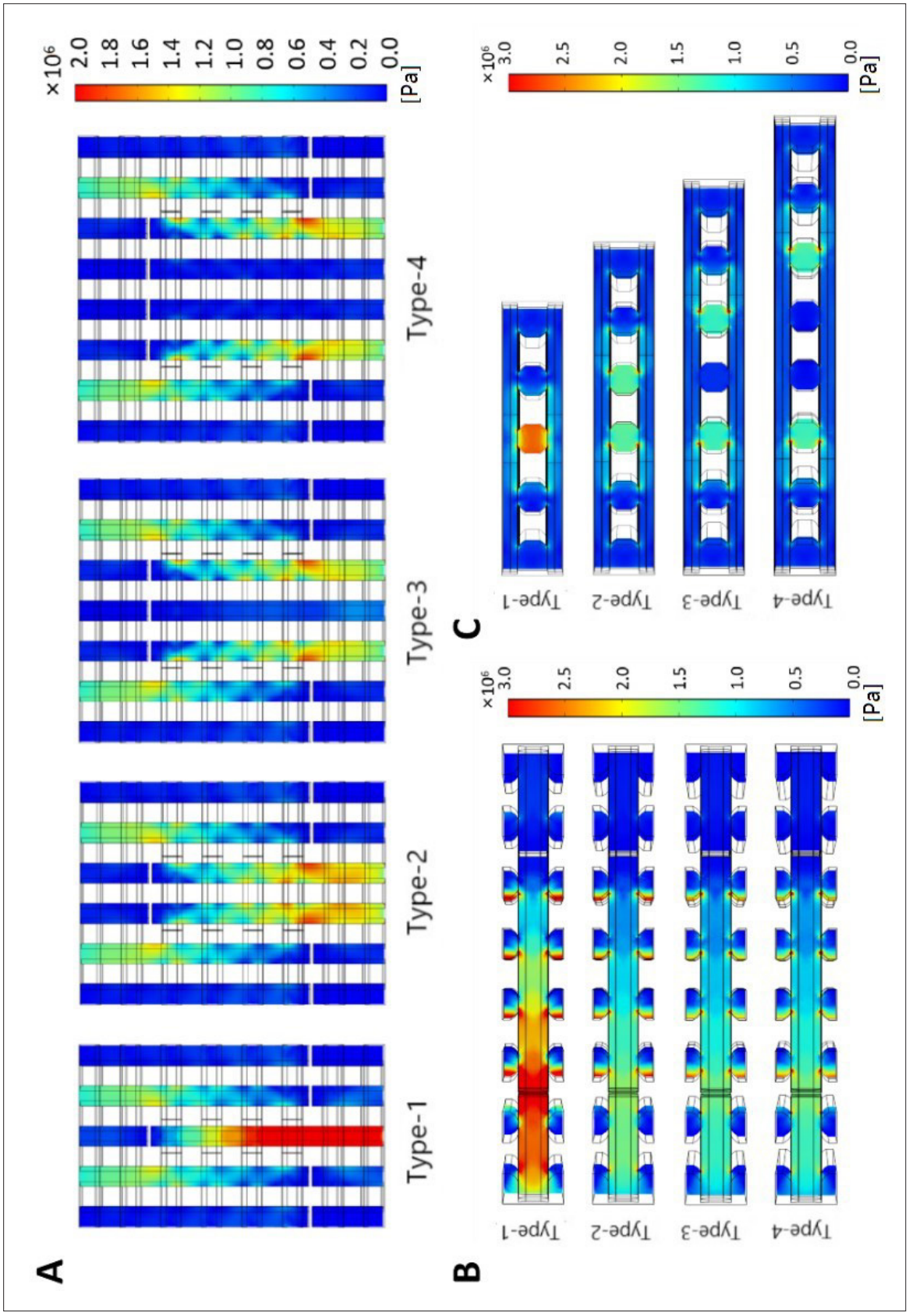

Figure S4. The stress contour plots of the first principal stress for structures with various widths of pin (*w*) in the tensile process. (A) Stress contour plots for the cross-section α. (B) Stress contour plots for the cross-section β. The greatest tensile stress is concentrated on the side farthest away from the boundary load. (C) Stress contour plots for the cross-section δ.

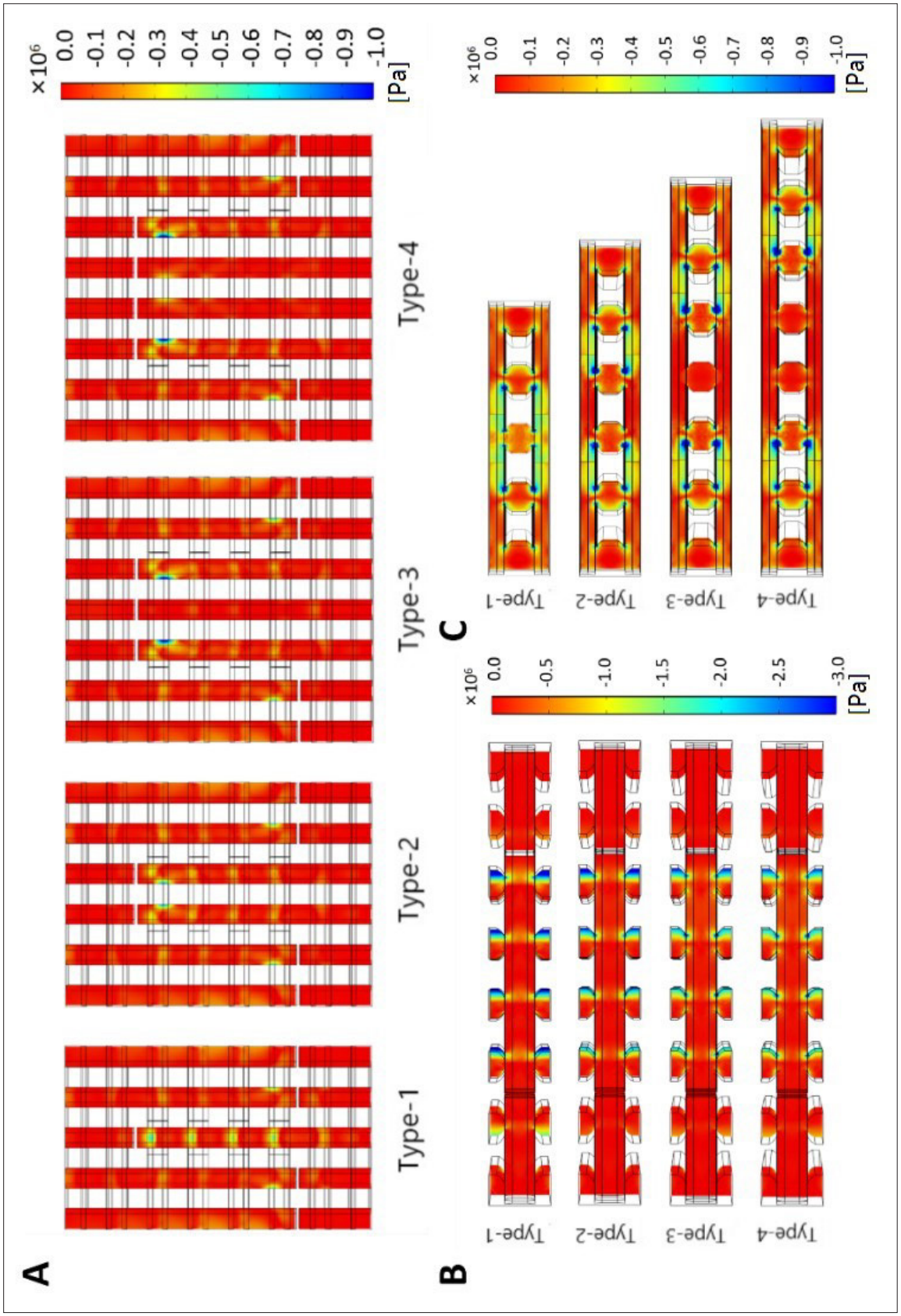

Figure S5. The stress contour plots of the third principal stress for structures with various widths of pin (w) in the tensile process. (A) Stress contour plots for the cross-section α. (B) Stress contour plots for the cross-section β. The greatest compressive stress is concentrated on the side farthest away from the boundary load. (C) Stress contour plots for the cross-section δ.

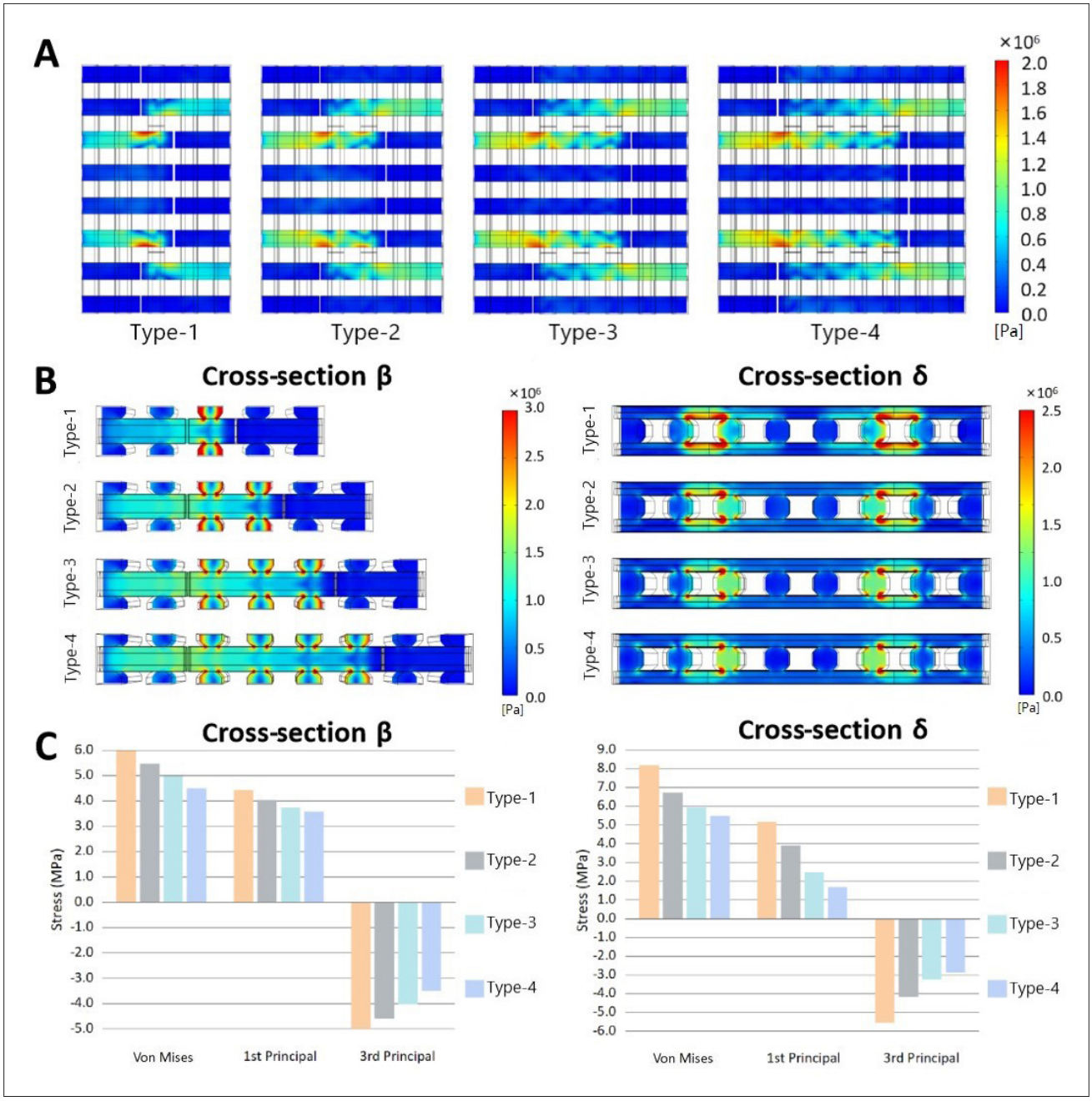

Figure S6. The stress contour plots of the von Mises stress for structures with various heights of pin (*h*) in the compression process. (A) Stress contour plots for the cross-section α. (B) Stress contour plots for the cross-section β and δ. Filaments near the bone–cartilage junction, which are along and perpendicular to the compressive direction, show a stress concentration at each fusion. (C) Comparison of stresses within the cross-sections β and δ for osteochondral interface scaffolds. With the increasing *h*, the maximum of von Mises stresses demonstrates a decrease.

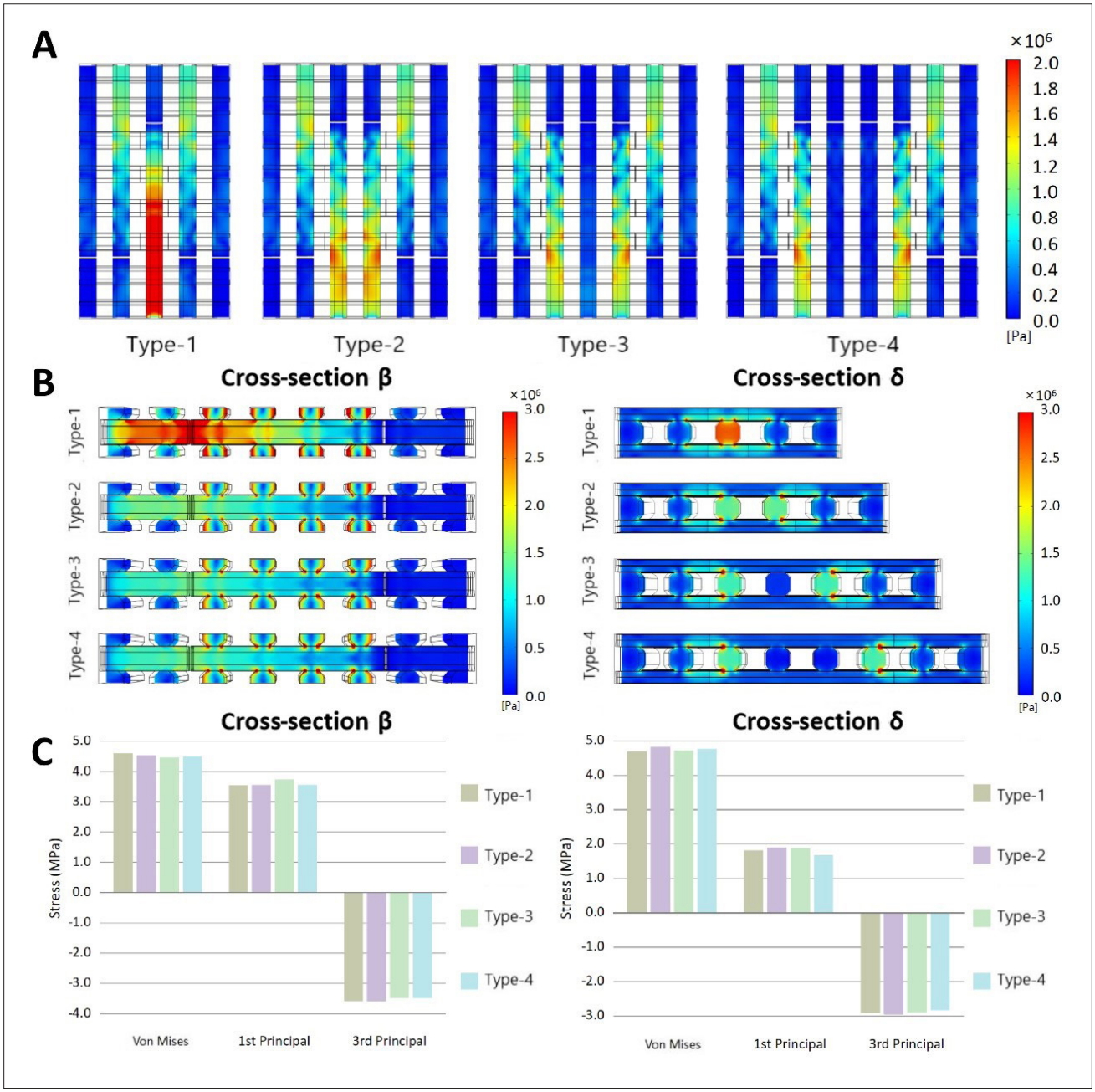

Figure S7. The stress contour plots of the von Mises stress for structures with various widths of pin (*w*) in the compression process. (A) Stress contour plots for the cross-section α. The von Mises stress concentrates at the outermost filaments of pins near the junction of bone and cartilage structures, and the scaffold of Type 1 shows higher stress at the central filament. (B) Stress contour plots for scaffolds at the cross-sections β and δ. Filaments that are perpendicular to the compressive direction demonstrate the stress concentration near the fusion of adjacent filaments. (C) Comparison of stresses within the cross-sections β and δ. With increasing *w*, the maximum von Mises stress remains constant.

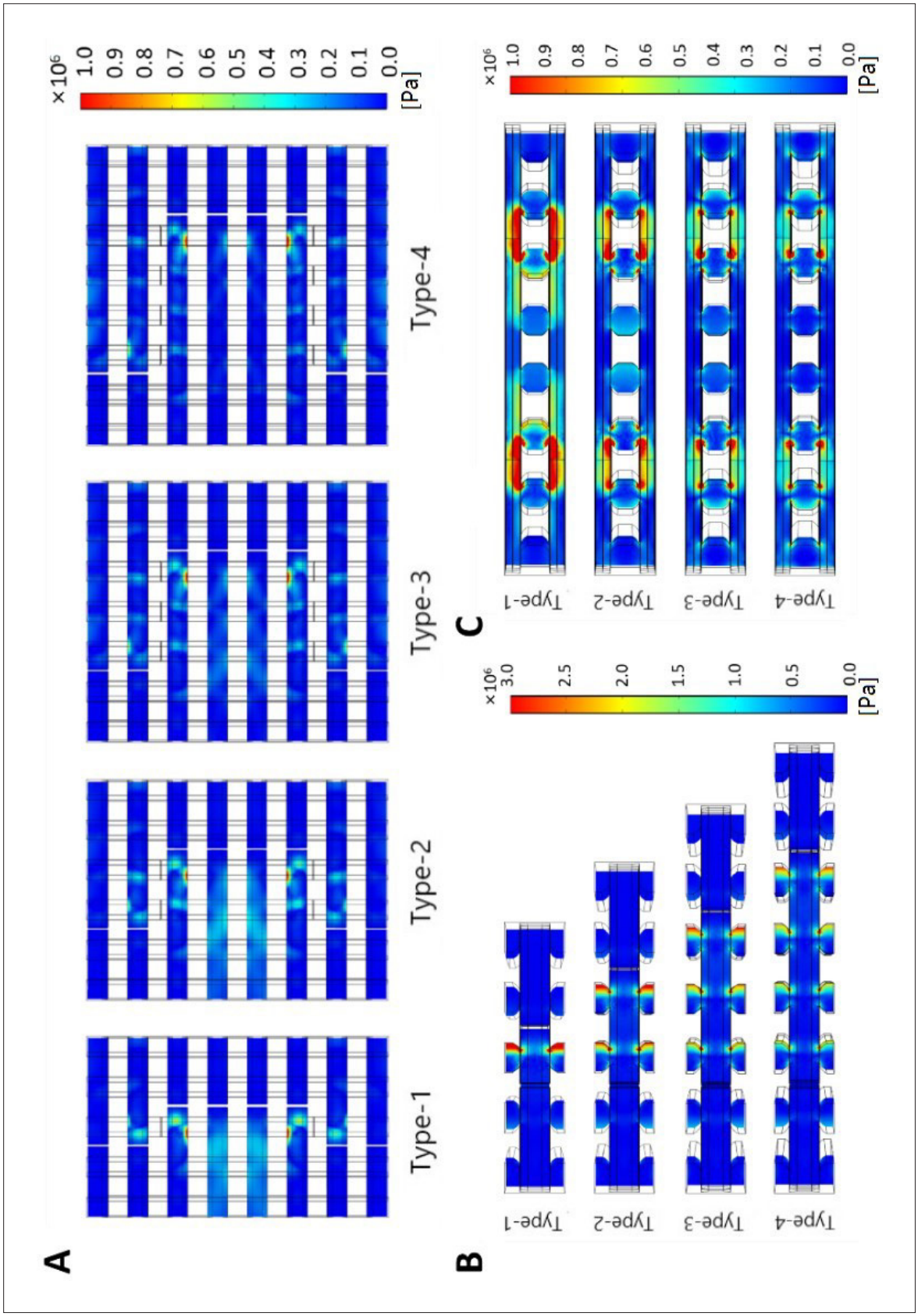

Figure S8. The stress contour plots of the first principal stress for structures with various heights of pin (*h*) in the compression process. (A) Stress contour plots for the cross-section α. (B) Stress contour plots for the cross-section β. (C) Stress contour plots for the cross-section δ. Filaments near the bone–cartilage junction, which are along and perpendicular to the compressive direction, show a stress concentration at each fusion.

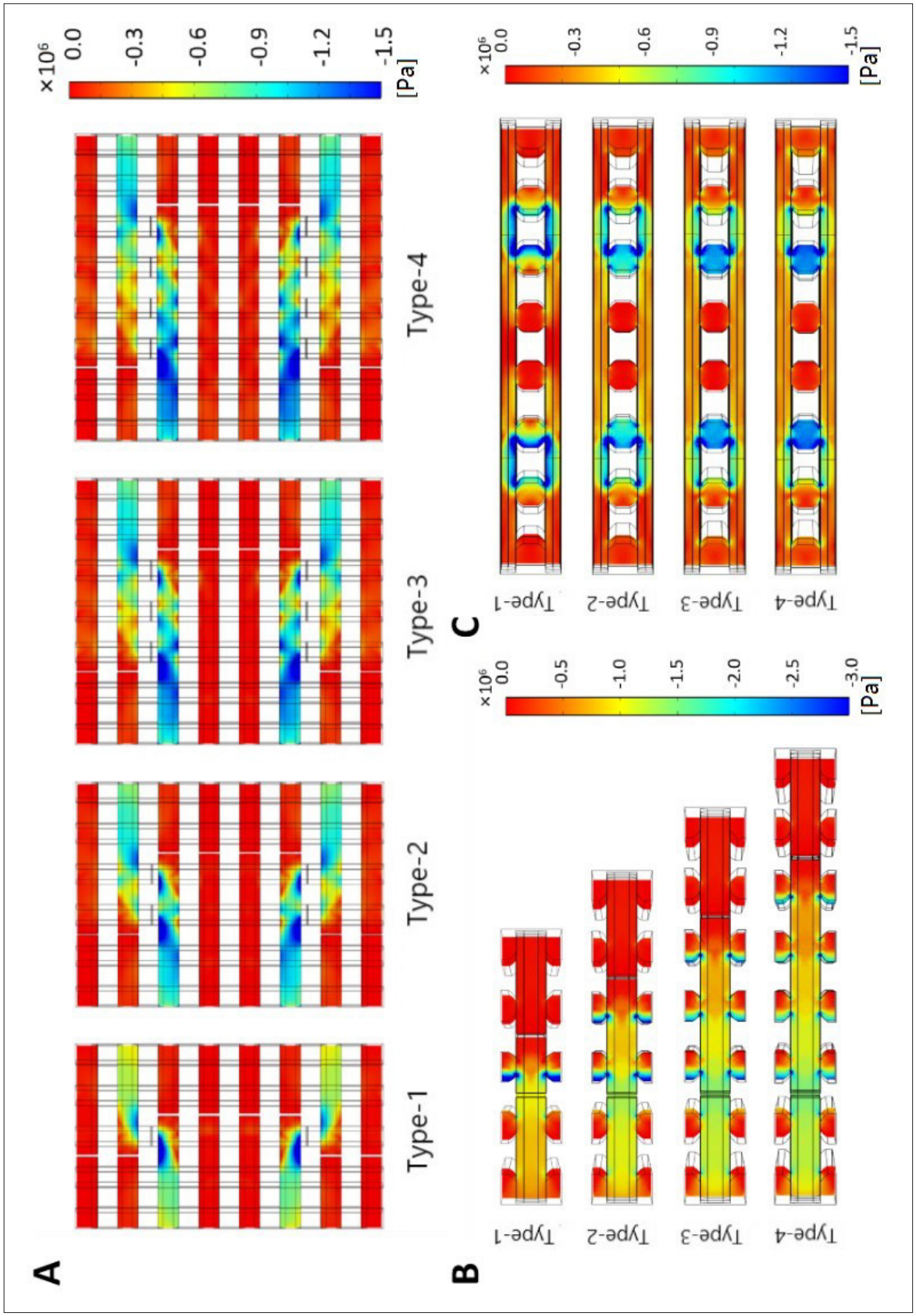

Figure S9. The stress contour plots of the third principal stress for structures with various heights of pin (*h*) in the compression process. (A) Stress contour plots for the cross-section α. (B) Stress contour plots for the cross-section β. (C) Stress contour plots for the cross-section δ. Filaments show a stress concentration at each fusion.

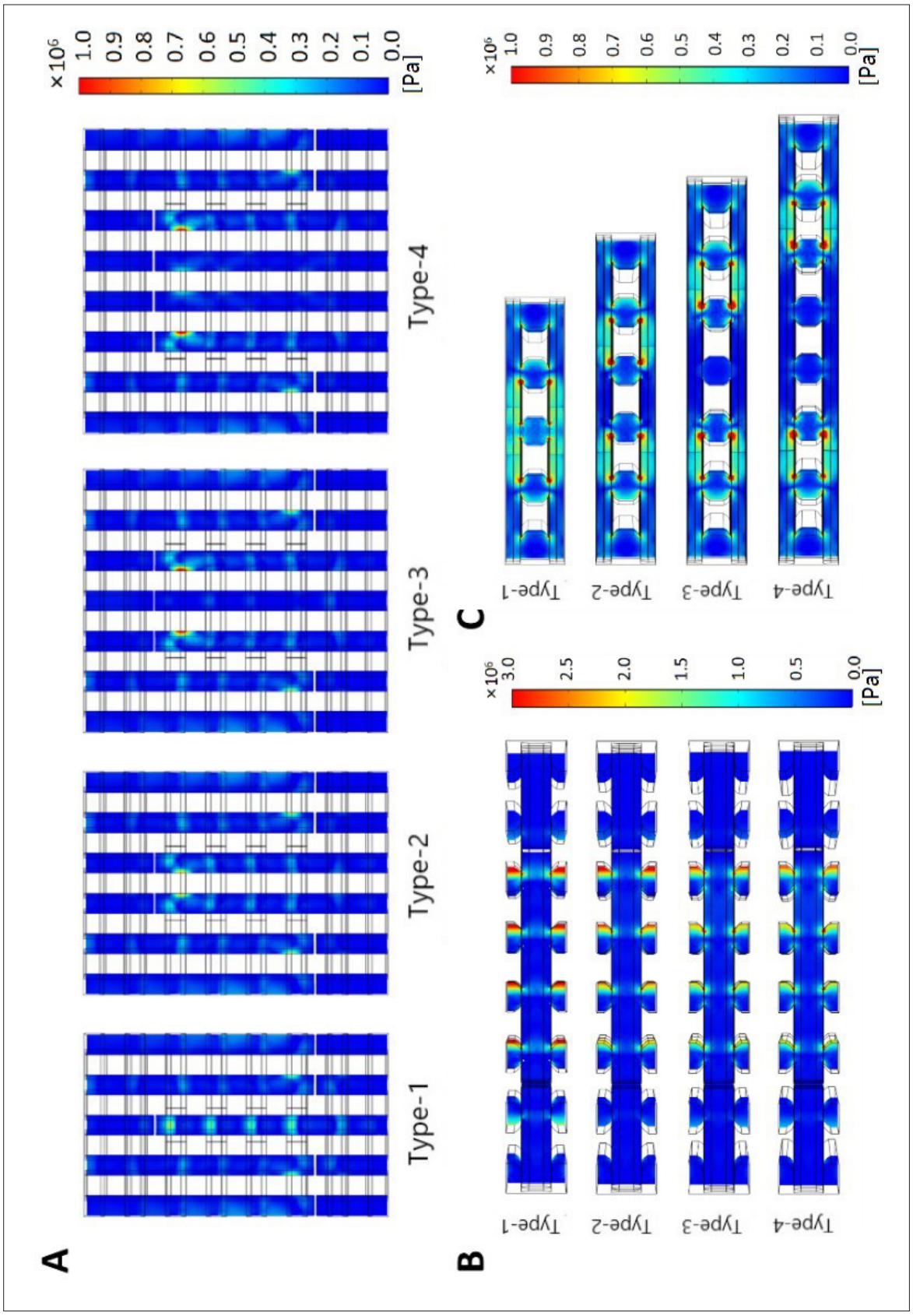

Figure S10. The stress contour plots of the first principal stress for structures with various widths of pin (*w*) in the compression process. (A) Stress contour plots for the cross-section α. (B) Stress contour plots for the cross-section β. The greatest tensile stress is concentrated on the side farthest away from the boundary load. (C) Stress contour plots for the cross-section δ.

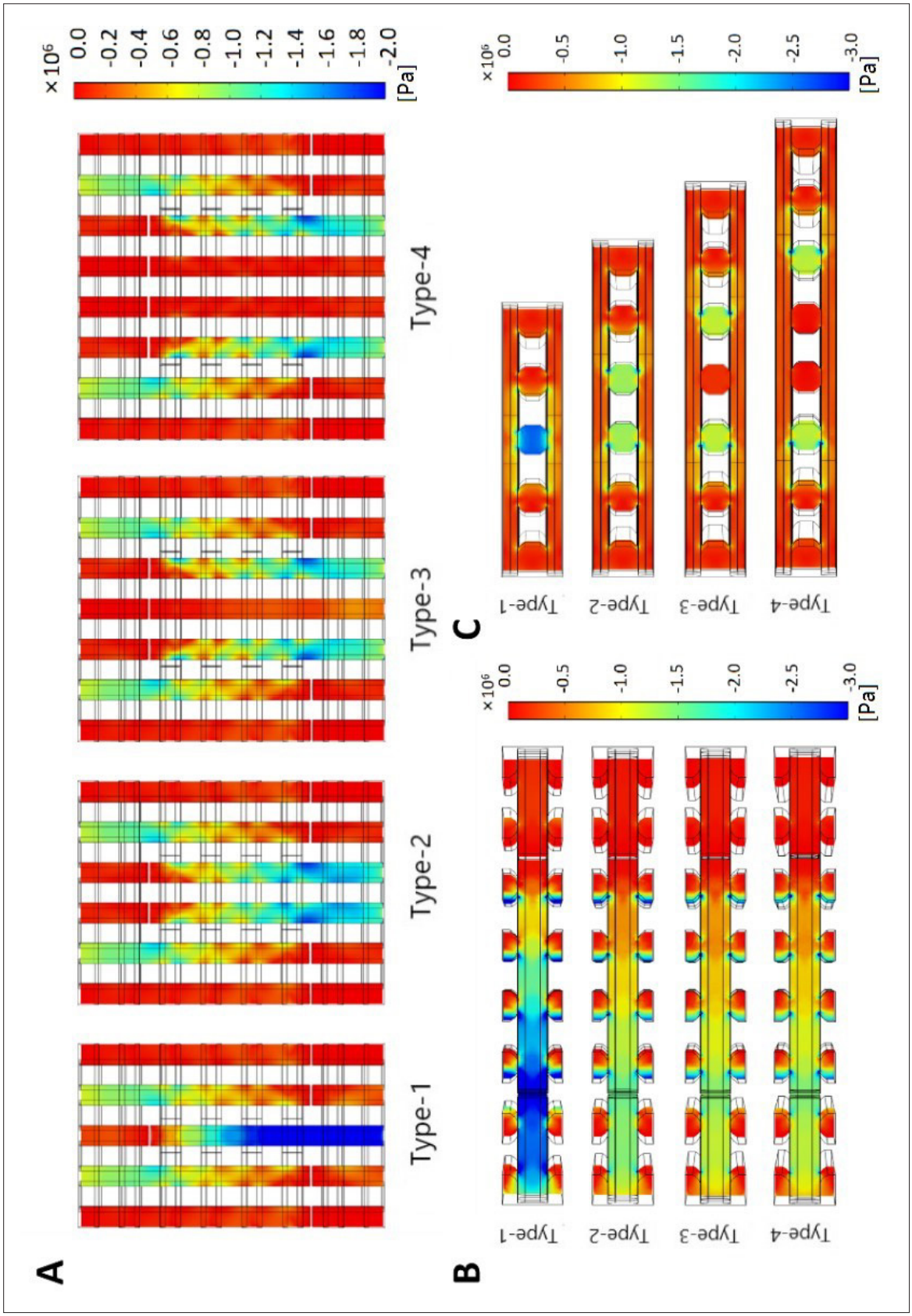

Figure S11. The stress contour plots of the third principal stress for structures with various widths of pin (w) in the compression process. (A) Stress contour plots for the cross-section α. (B) Stress contour plots for the cross-section β. The greatest compressive stress is concentrated on the side farthest away from the boundary load. (C) Stress contour plots for the cross-section δ.

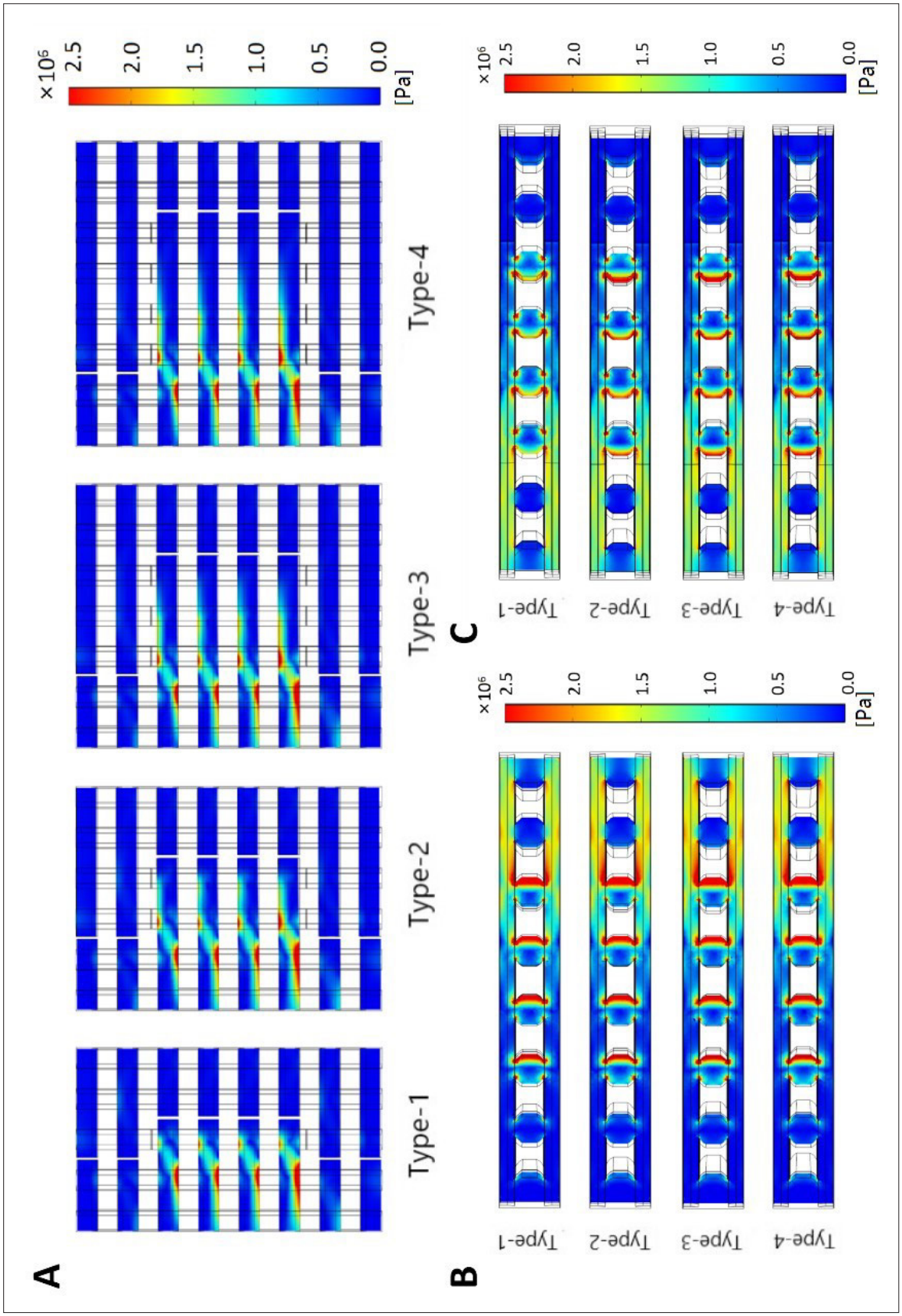

Figure S12. The stress contour plots of the first principal stress for structures with various heights of pin (*h*) in the shearing process. (A) Stress contour plots for the cross-section α. (B) Stress contour plots for the cross-section γ. (C) Stress contour plots for the cross-section δ.

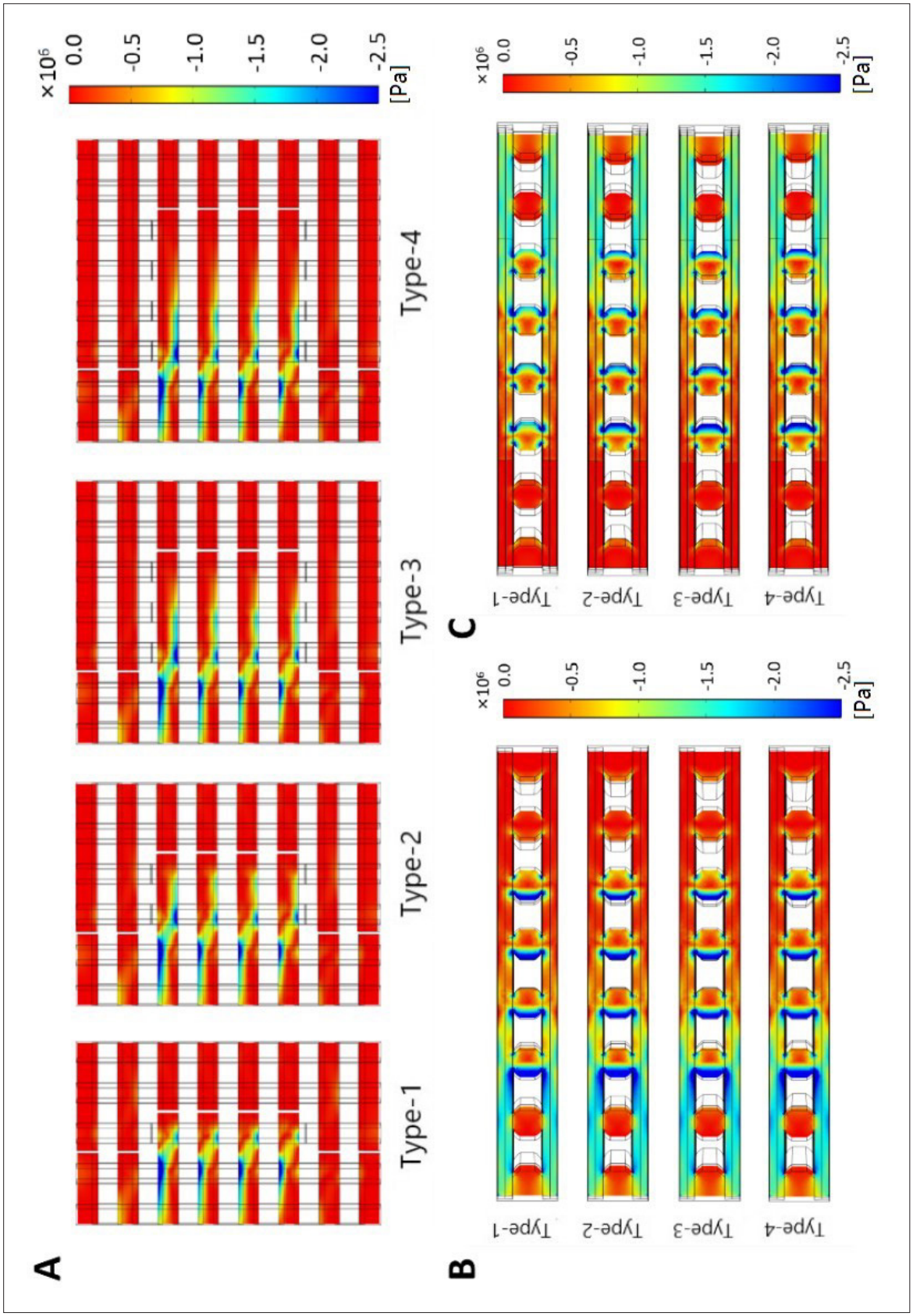

Figure S13. The stress contour plots of the third principal stress for structures with various heights of pin (*h*) in the shearing process. (A) Stress contour plots for the cross-section α. (B) Stress contour plots for the cross-section γ. (C) Stress contour plots for the cross-section δ.

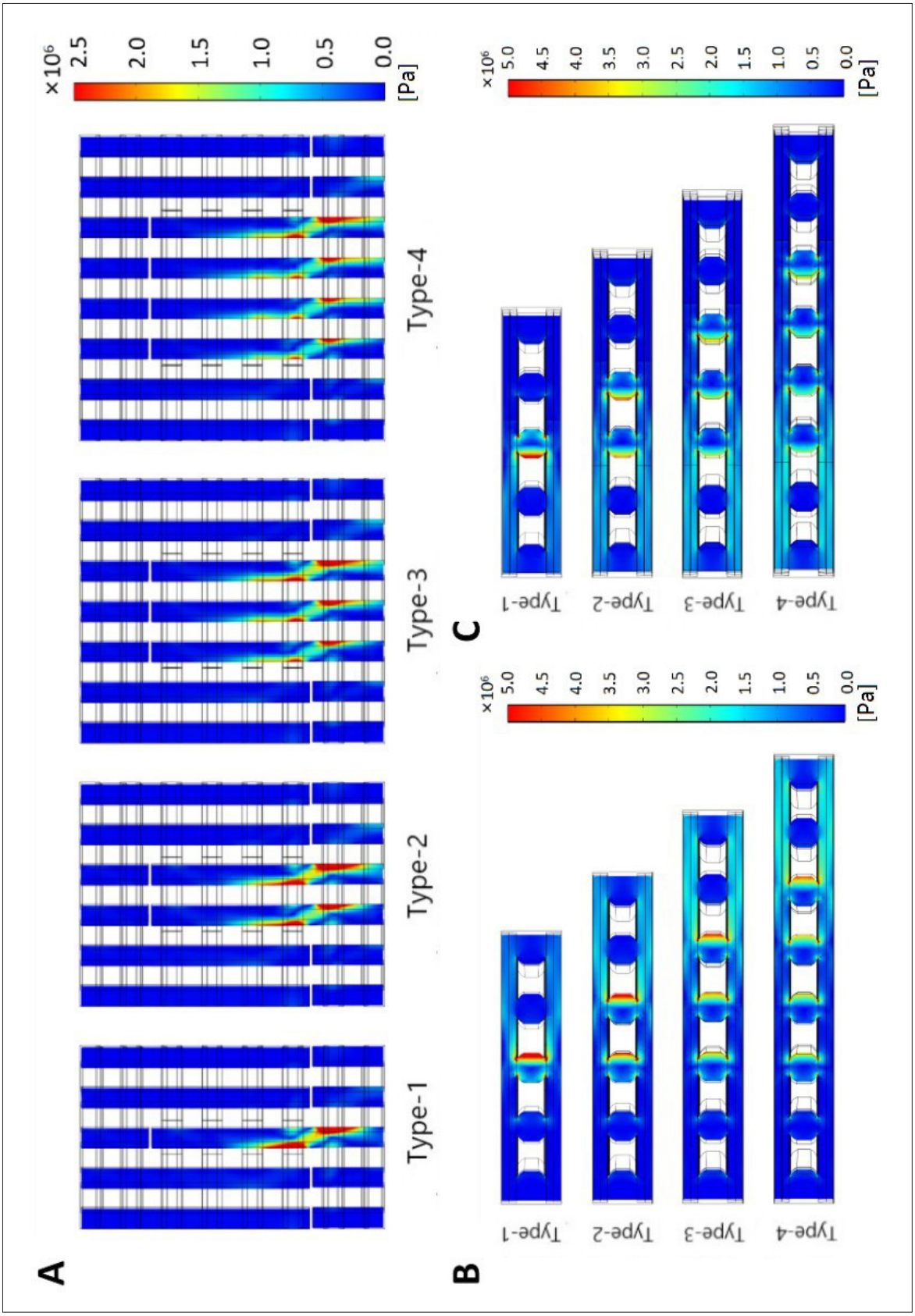

Figure S14. The stress contour plots of the first principal stress for structures with various widths of pin (*w*) in the shearing process. (A) Stress contour plots for the cross-section α. (B) Stress contour plots for the cross-section γ. (C) Stress contour plots for the cross-section δ.

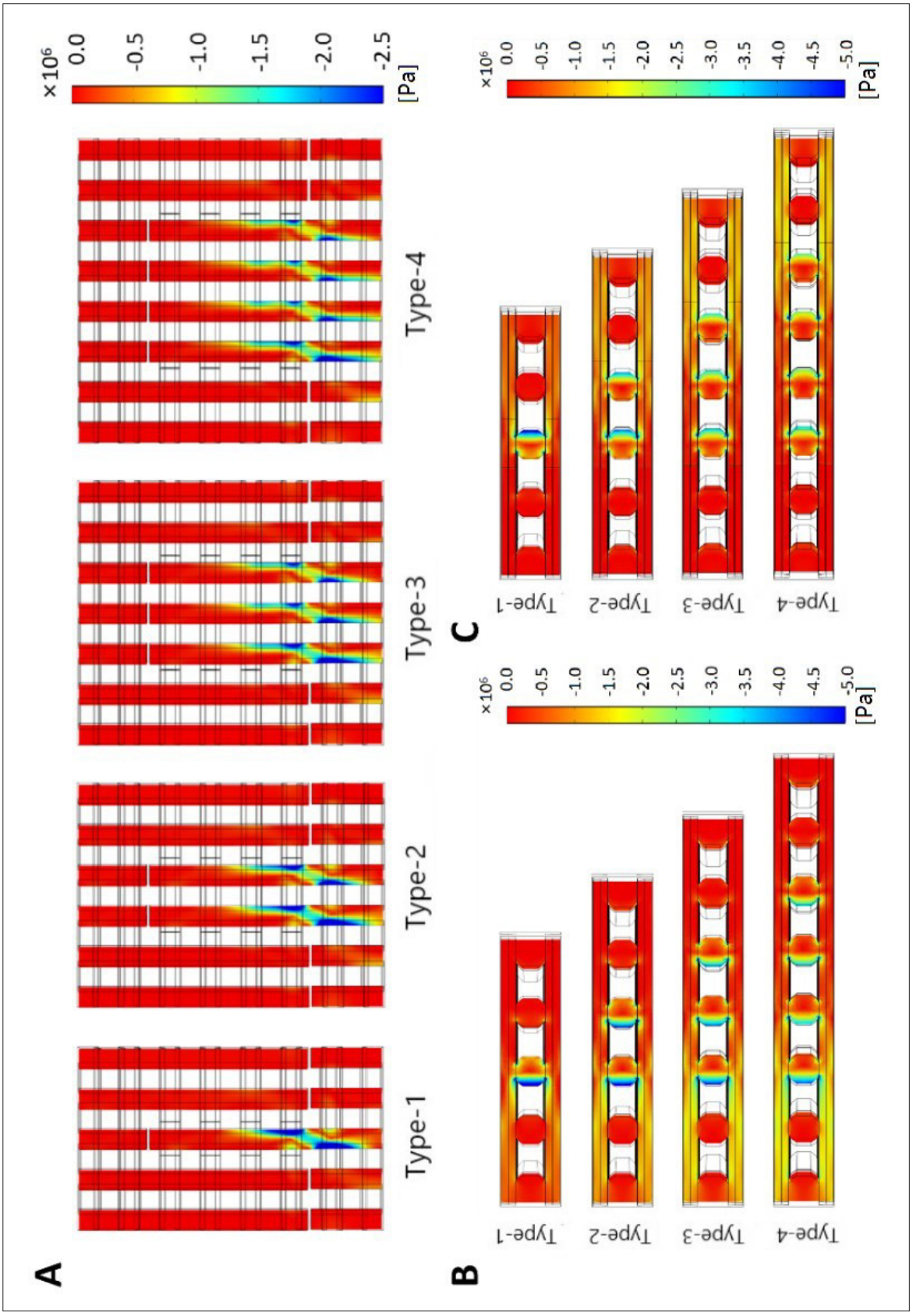

Figure S15. The stress contour plots of the third principal stress for structures with various widths of pin (*w*) in the shearing process. (A) Stress contour plots for the cross-section α. (B) Stress contour plots for the cross-section γ. (C) Stress contour plots for the cross-section δ.

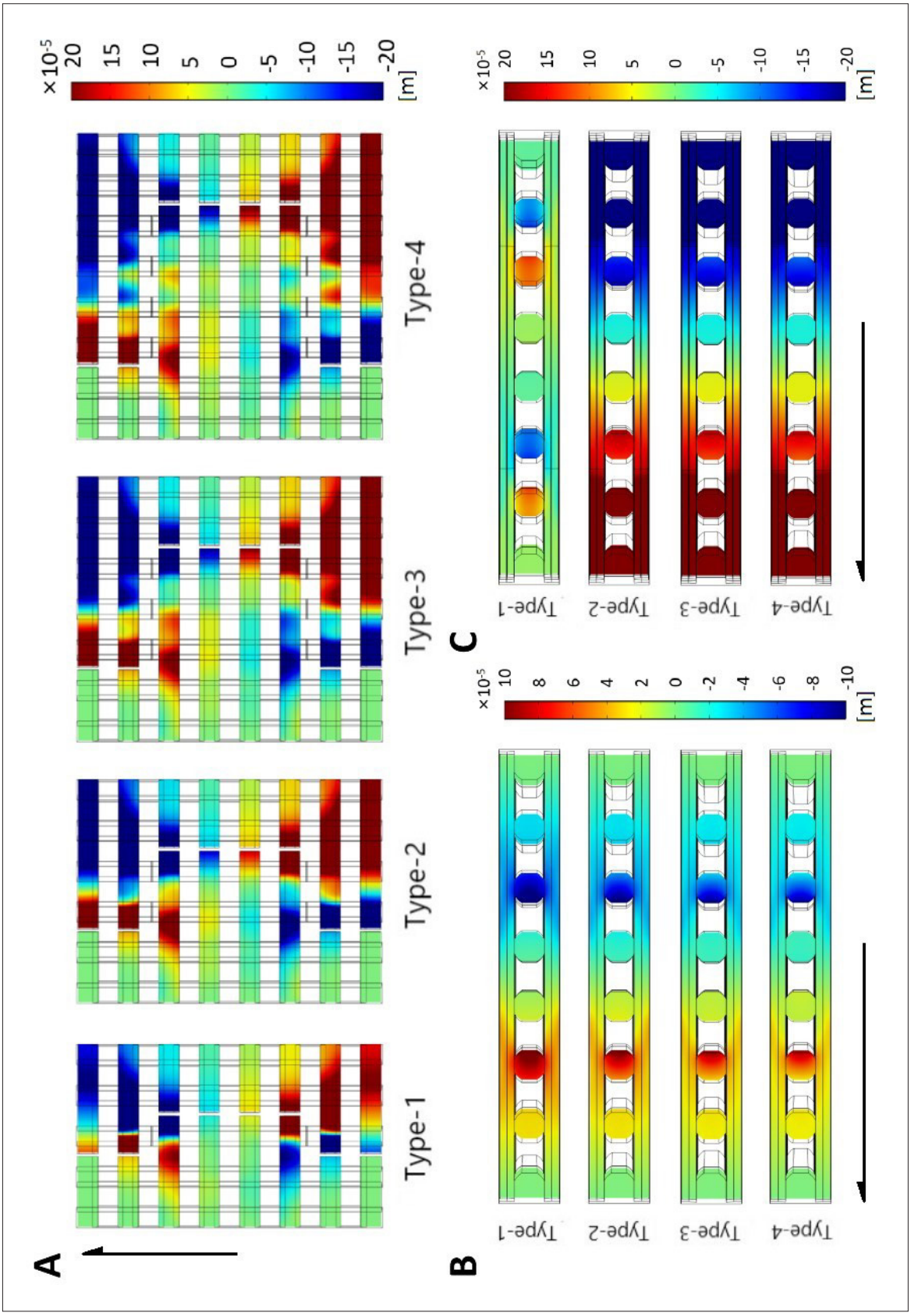

Figure S16. The deformation contour plots for structures with various heights of pin (*h*) in the tensile process. The positive direction of deformation has been indicated. (A) Deformation contour plots for the cross-section α. (B) Deformation contour plots for the cross-section γ. (C) Deformation contour plots for the cross-section δ.

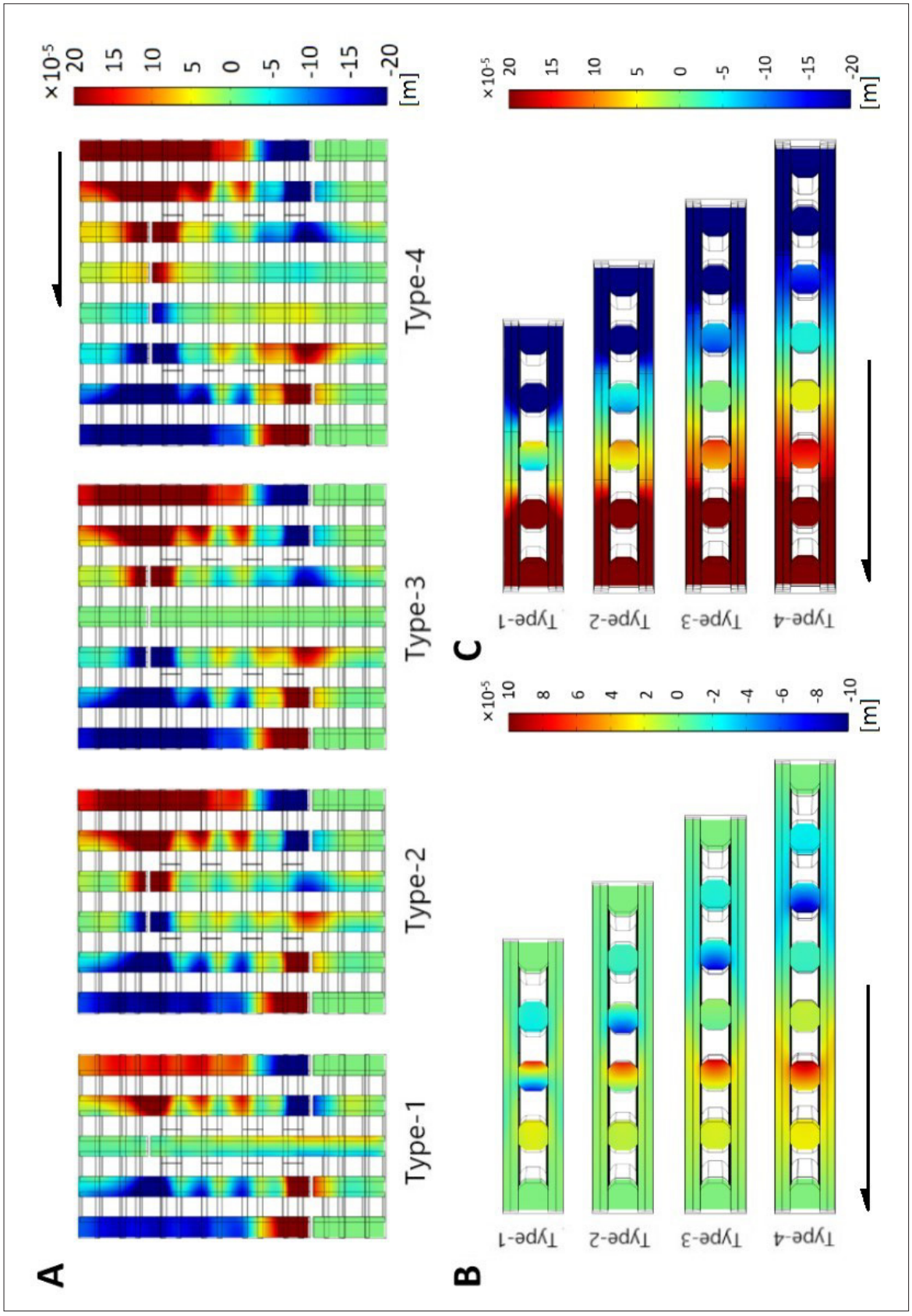

Figure S17. The deformation contour plots for structures with various widths of pin (w) in tensile process. The positive direction of deformation has been indicated. (A) Deformation contour plots for the cross-section α. (B) Deformation contour plots for the cross-section γ. (C) Deformation contour plots for the cross-section δ.

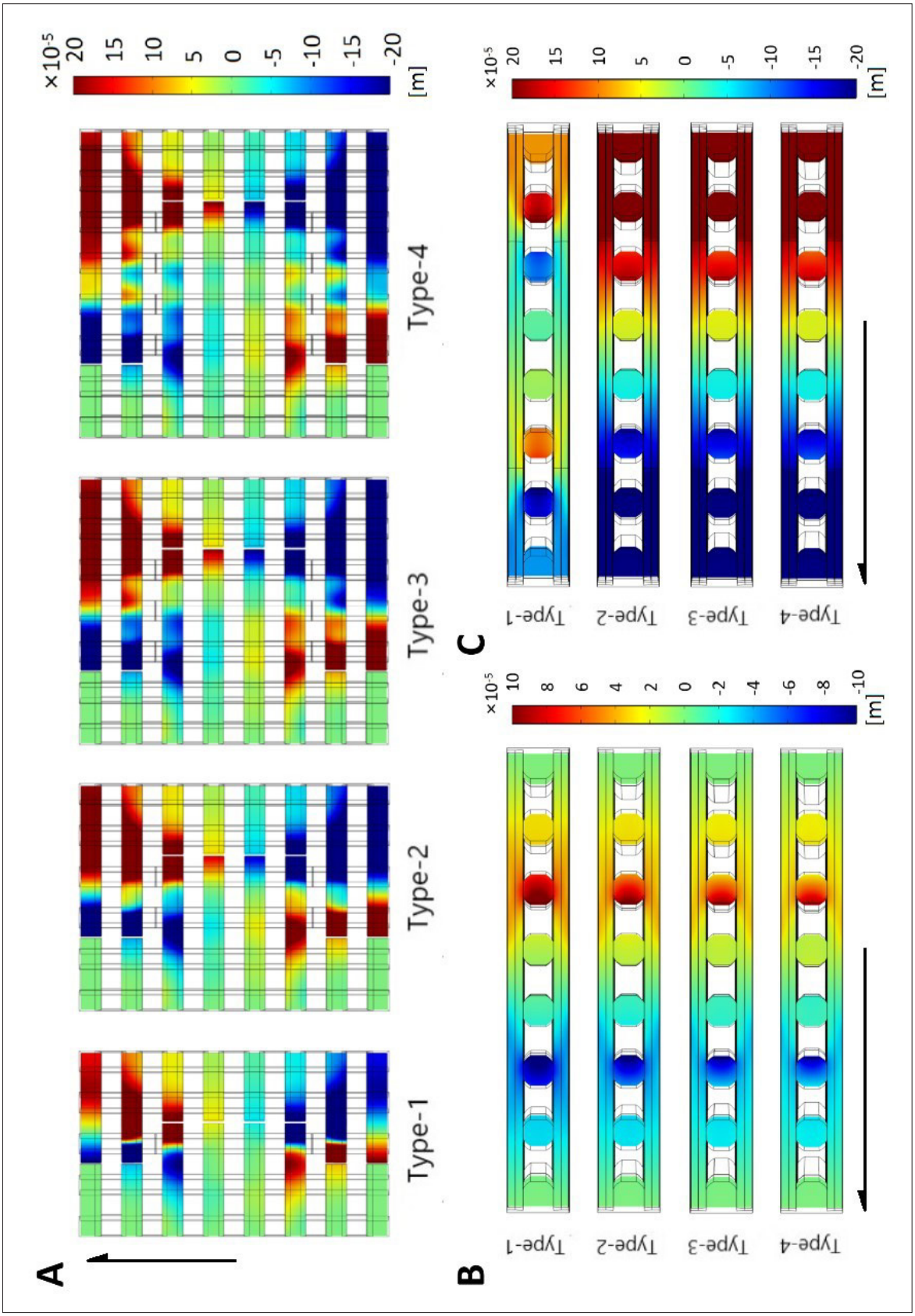

Figure S18. The deformation contour plots for structures with various heights of pin (*h*) in the compression process. The positive direction of deformation has been indicated. (A) Deformation contour plots for the cross-section α. (B) Deformation contour plots for the cross-section γ. (C) Deformation contour plots for the cross-section δ.

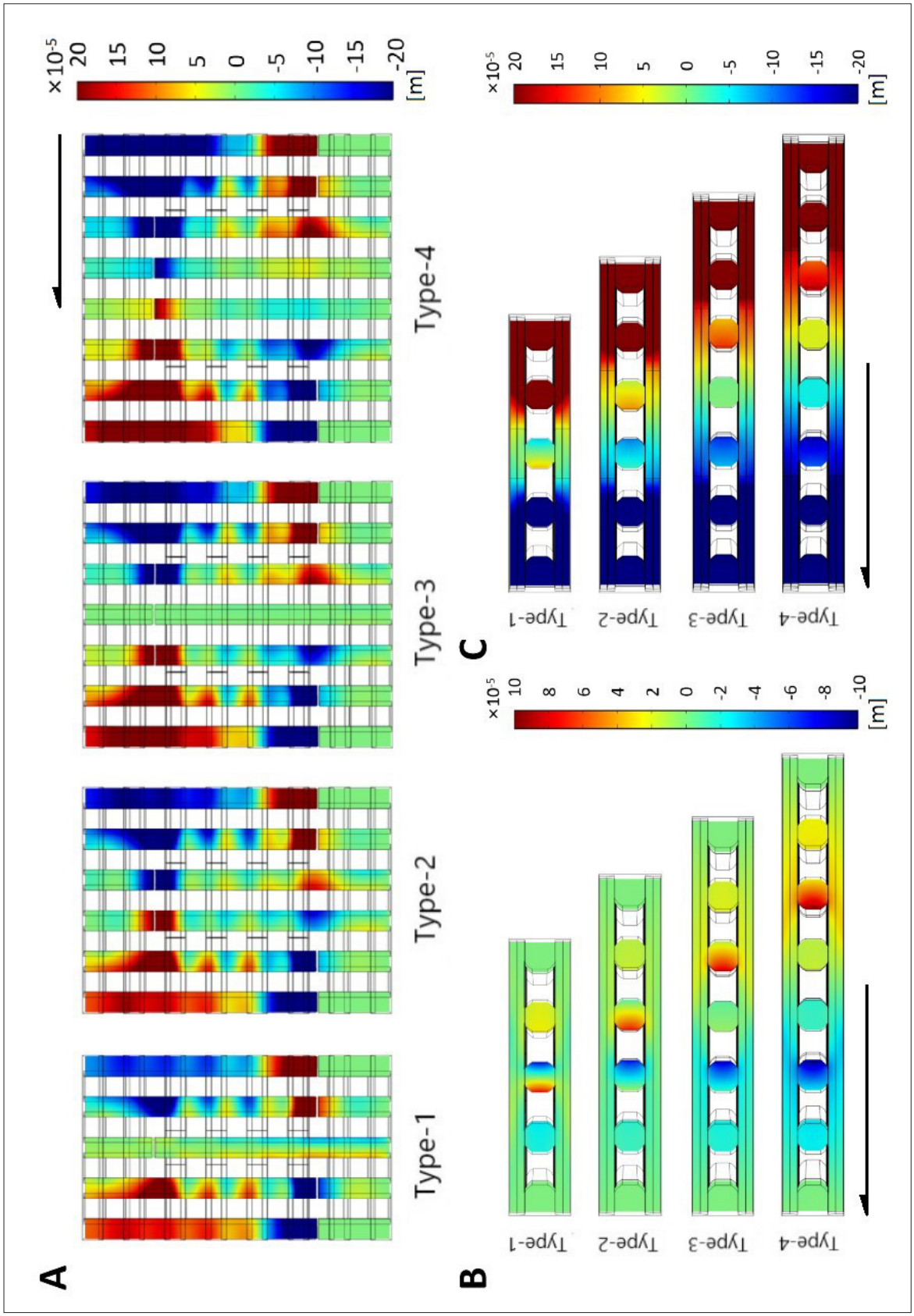

Figure S19. The deformation contour plots for structures with various widths of pin (w) in the compression process. The positive direction of deformation has been indicated. (A) Deformation contour plots for the cross-section α. (B) Deformation contour plots for the cross-section γ. (C) Deformation contour plots for the cross-section δ.

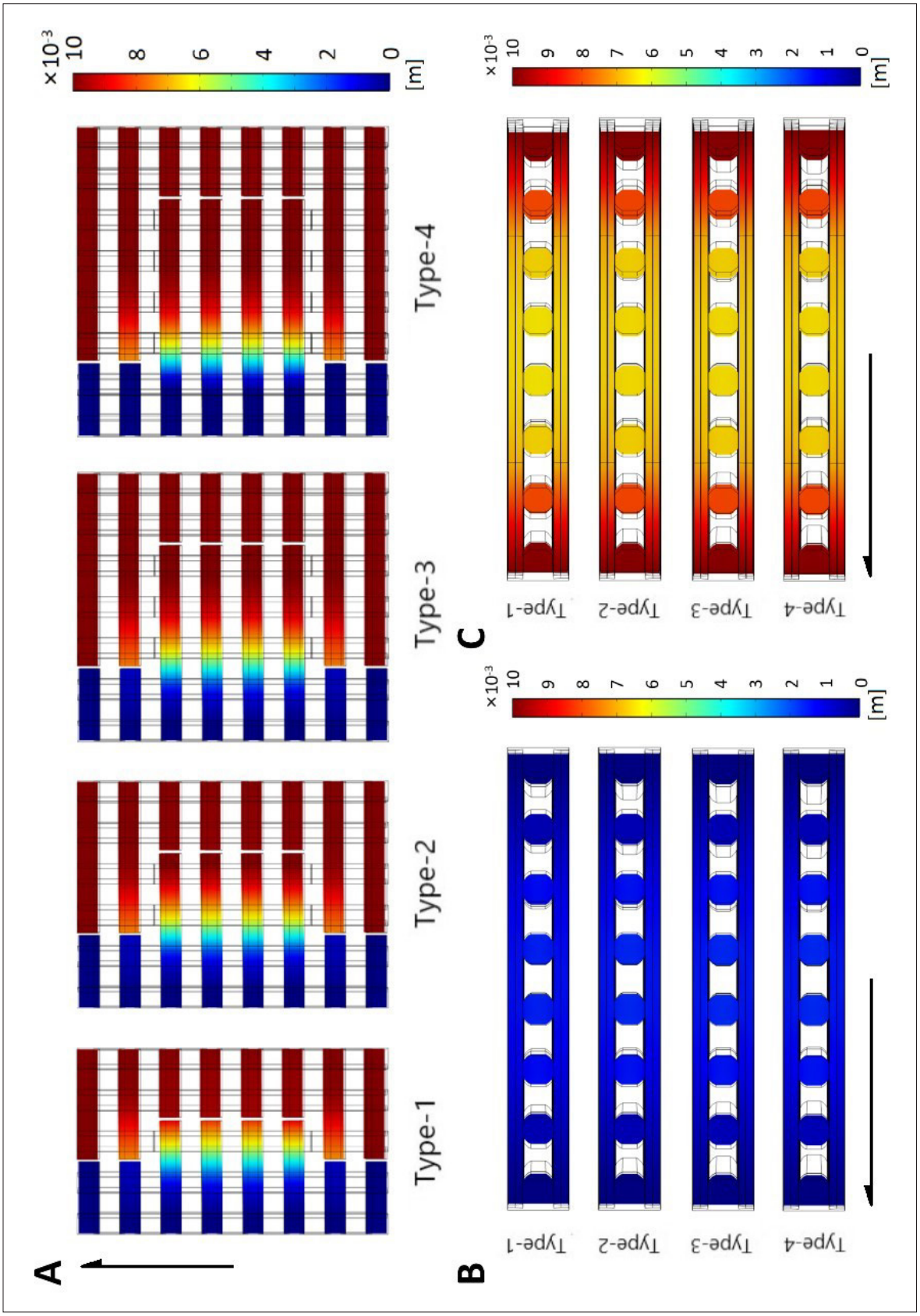

Figure S20. The deformation contour plots for structures with various heights of pin (*h*) in the shear process. The positive direction of deformation has been indicated. (A) Deformation contour plots for the cross-section α. (B) Deformation contour plots for the cross-section γ. (C) Deformation contour plots for the cross-section δ.

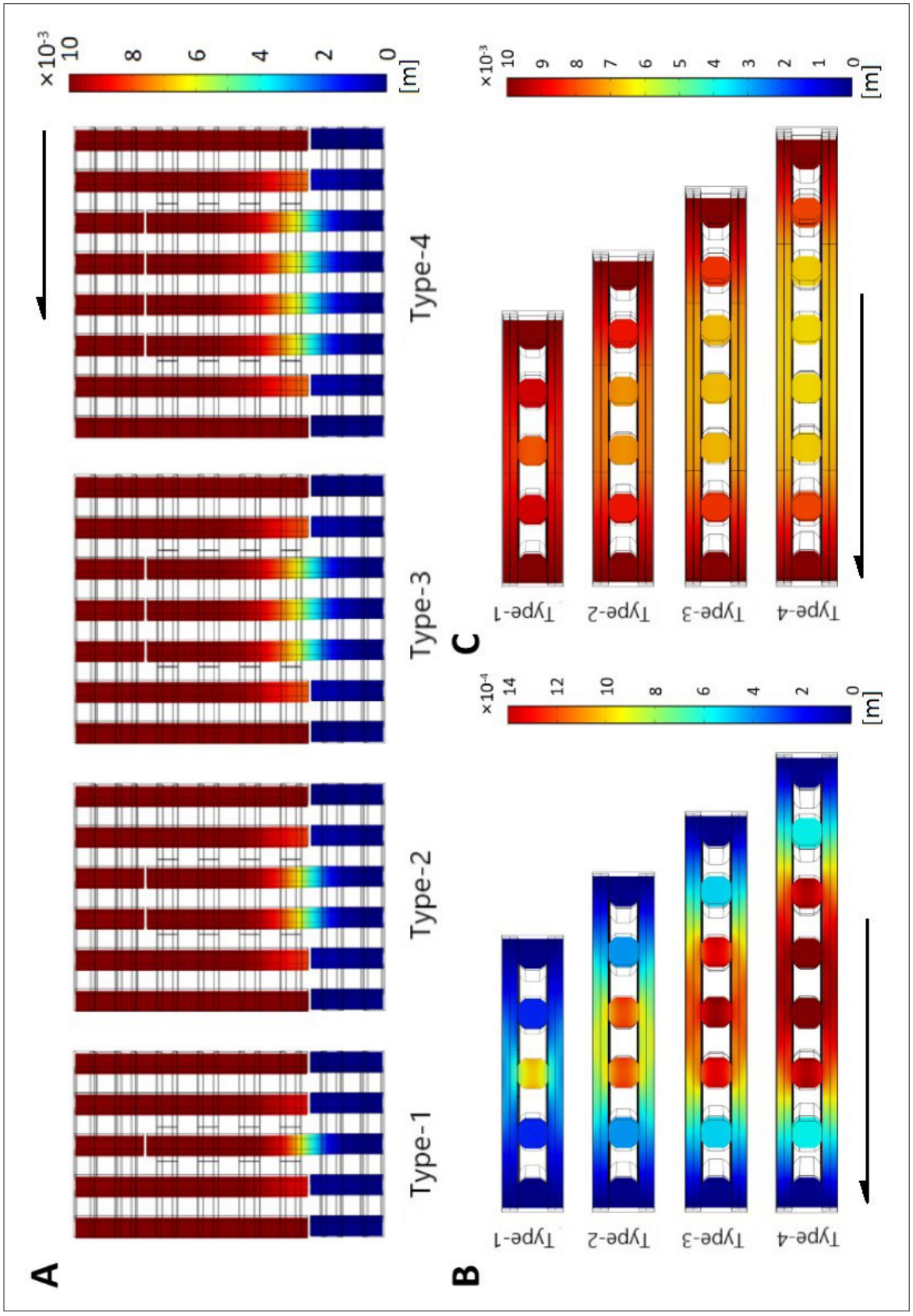

Figure S21. The deformation contour plots for structures with various widths of pin (w) in the shear process. The positive direction of deformation has been indicated. (A) Deformation contour plots for the cross-section α. (B) Deformation contour plots for the cross-section γ. (C) Deformation contour plots for the cross-section δ.